

tissue affected by malignant, neurologic,

traumatic, infectious, or congenital con-

ditions. Lower urinary tract (LUT) reconstructive surgeries, such as neobladder cre-

ation, augmentation cystoplasty, and prox-

imal hypospadias repair, are high-risk and

complex procedures. Recent studies re-

port complication rates of 33-68%, in part

due to abnormal or inadequate local bladder or urethral tissue.<sup>[1]</sup> In such cases,

secondary tissue sources are required.

However, current gold-standard autologous

grafts, such as the foreskin, buccal mu-

cosa, or bowel, have limited availability, pos-

sess undesirable tissue properties (e.g., mu-

cous production and solute absorption by the bowel), and increase the risk of donor

site morbidity.[2] Thus, there is an ongo-

ing need for tissue alternatives with op-

timized biological and mechanical prop-

# Biomimetic, Suturable, and Extensible Electrospun Scaffolds for Lower Urinary Tract Surgical Reconstruction

Renea M. Sturm,\* Yadi Huo, Felix Yiu, Yimin Gu, Ronak Afshari, Zijian Zhong, Ruby Jimenez, Rebekah Jung, Aljohn Cabuan, Keshav Shukla, Karen Harrison, Judy Su, George E. Aninwene II, Victoria Lee, Mahsa Ghovvati, Kaavian Shariati, Nicholas Jackson, Song Li, and Nasim Annabi\*

Common autologous tissue sources used for the repair or replacement of lower urinary tract (LUT) organs include the inner cheek (buccal), small and large bowels, and foreskin. These sources have limited availability, introduce the risk of donor site complications, and differ mechanically and biologically from LUT tissue. To address this, fibrous composite scaffolds with varying ratios of two naturally derived polymers—gelatin methacryloyl and an elastin-like peptide are fabricated via electrospinning and photo-crosslinking. Among the tested ratios, 5:5% (w/v) elastin-like peptide-gelatin methacryloyl (5E5G) fibrous scaffolds are suturable and most closely replicate LUT tissue, exhibiting a tensile modulus of 25.6  $\pm$  4.77 kPa, an ultimate tensile strength of 41  $\pm$  6.68 kPa, and an elongation of 167.4%  $\pm$  5.41%. Furthermore, the 5E5G scaffold exhibits a mean degradation exceeding 50% after 21 days in 37 °C Dulbecco's Phosphate Buffered Saline. In vitro, smooth muscle and fibroblast proliferation is robust on both 0E10G and 5E5G scaffolds, whereas urothelial cells display lower relative proliferation. In vivo subcutaneous implantation in rats demonstrates biocompatibility and supports tissue ingrowth without local fibrosis or inflammatory responses, similar to a sham injury model. Collectively, 5E5G electrospun scaffolds represent promising substrates for enhancing LUT tissue regeneration.

erties to support healthy LUT regeneration.

erties to support healthy LUT regeneration, thereby enabling an early return of function and reducing post-operative morbidity. Historically, LUT tissue engineering has been successfully used to replace or repair urethral or bladder tissues in healthy small animal models. However, in larger animal and human models, engineered constructs show limited translatability

#### 1. Introduction

Engineered biomimetic materials offer an alternative to autologous grafts for the repair or replacement of bladder or urethral

R. M. Sturm, F. Yiu, R. Jimenez, R. Jung, A. Cabuan, K. Shukla, K. Harrison, G. E. Aninwene II, V. Lee, K. Shariati Department of Urology, Division of Pediatric Urology David Geffen School of Medicine University of California Los Angeles Los Angeles, CA 90095, USA E-mail: rsturm@mednet.ucla.edu

The ORCID identification number(s) for the author(s) of this article can be found under https://doi.org/10.1002/adhm.202500651

© 2025 The Author(s). Advanced Healthcare Materials published by Wiley-VCH GmbH. This is an open access article under the terms of the Creative Commons Attribution-NonCommercial-NoDerivs License, which permits use and distribution in any medium, provided the original work is properly cited, the use is non-commercial and no modifications or adaptations are made.

DOI: 10.1002/adhm.202500651

Y. Huo, Y. Gu, R. Afshari, Z. Zhong, M. Ghovvati, N. Annabi Department of Chemical and Biomolecular Engineering University of California Los Angeles Los Angeles, CA 90095, USA

E-mail: nannabi@ucla.edu

J. Su

California NanoSystems Institute University of California Los Angeles Los Angeles, CA 90095, USA

N. Jackson Department of Medicine Statistics Core David Geffen School of Medicine University of California Los Angeles Los Angeles, CA 90024, USA S. Li, N. Annabi

Department of Bioengineering
University of California Los Angeles
Los Angeles, CA 90095, USA





www.advhealthmat.de

owing to a lack of vascularization and tissue regeneration, inconsistent functional outcomes, and the need for repeat surgical reconstruction. [4] The most common historical approach in LUT tissue engineering has been the application of decellularized matrices (dECM) to enhance tissue regeneration. [4] However, these biological scaffolds exhibit tensile and structural properties that differ substantially from those of native LUT tissue. [5] Furthermore, acellular matrices exhibit limited reproducibility owing to variability at the organism, tissue, and processing levels. [6] To date, no mechanically matched United States Food and Drug Administration (FDA)-approved clinical products are available for LUT tissue repair or replacement.

The pronounced differences in the tensile properties of current autografts and engineered substrates compared with those of native LUT tissue have both microscopic and macroscopic effects following surgical reconstruction. At the microscopic level, the mechanical niche is a critical parameter in the control of cell fate and extracellular matrix (ECM) deposition.<sup>[7]</sup> In addition, tissue mechanics and topography affect wound healing, as well as cell ingrowth, morphology, and phenotype.[8] In the urinary tract, low-density polarized collagen grafts with tensile properties matching those of native tissue have been shown to improve smooth muscle cell (SMC) regeneration and patency compared with high-density grafts in urethroplasty animal models.<sup>[9]</sup> Furthermore, wound healing and immune responses, including macrophage phenotypes, can be altered by the bladder ECM structure, mechanics, and biological modifications that occur in disease states.[10] At the macroscopic level, the extensibility of bladder and urethral tissue is crucial for normal cyclic voiding.[11] Both tissue-based and surgical factors can compromise surgical anastomoses, leading to complications such as urine leaks, infection, and dehiscence, which necessitate prolonged catheterization.[12] Therefore, future substrates intended for LUT reconstructive procedures must address both the macroscopic and microscopic effects of biomaterial mechanics and structure.

Biomaterial selection and fabrication are critical for developing ECM-like microenvironments that enhance tissue regeneration. The high water content and permeability of hydrogels are applied to mimic native tissue microenvironments.<sup>[13]</sup> Emerging techniques, such as three-dimensional (3D) hydrogel cultures combined with microscale technologies, highlight the importance of the surface topography, porosity, and fibrous architecture in directing and enhancing tissue neovascularization and regeneration.<sup>[14]</sup> However, their clinical applications are often limited by their inadequate mechanical properties and unpredictable degradation rates.<sup>[15]</sup> In this regard, hybrid hydrogels can optimize the mechanical properties and biological activities of the resultant biomimetic scaffolds, improving their applicability for intended medical applications.<sup>[16]</sup> Moreover, compared with hydrogels with a single-polymer network, hybrid hydrogels more effectively emulate the versatile properties of native physiological microenvironments.[17]

Electrospinning, in which a fibrous mat can be created by extruding polymer solutions onto a surface using a high-voltage electric field, is a fabrication method used to enhance the topographical control and stretchability of constructs based on the material selection and fiber alignment. In the LUT, electrospun scaffolds show promise when composed of biologic or

synthetic biomaterials such as collagen, silk fibroin, polylactic acid, and poly(L-lactide-co- $\epsilon$ -caprolactone), respectively. [18] Hybrid scaffolds combining naturally derived and synthetic polymers are also engineered to improve biomechanical properties while maintaining their regenerative potential. [19] Furthermore, in vitro testing with progenitor cells, with or without small molecules, demonstrates potential to enhance wound healing and minimize post-operative strictures in small animal models. [18] However, challenges persist regarding scaffold mechanical strength, suturability, in vivo degradation rates, and applicability in complex or large LUT defects.

To address the need for biomimetic, non-immunogenic, degradable, suturable, and mechanically matched scaffolds that promote the proliferation of LUT cell lines and tissue regeneration, a photo-crosslinked, suturable, elastic fibrous mat composed of gelatin methacryloyl (GelMA) and an elastin-like peptide (ELP) sequence is developed using electrospinning for scaffold fabrication. GelMA, which contains inherent Arg-Gly-Asp (RGD) sequences, supports cell adhesion, [20] whereas its modification with methacrylic anhydride enables tunable mechanics and biodegradation.[21] ELP, a recombinant analog of natural elastin, is biocompatible, biodegradable, and possesses an intrinsic structural disorder that contributes to elasticity.<sup>[22]</sup> In this study, electrospun porous ELP-GelMA composite hydrogels are designed to reproduce the mechanical properties of the LUT. In vitro evaluation using SMC, urothelial (UC), and fibroblast (Fib) cell lines assesses scaffold cytocompatibility. Finally, rat implantation studies are performed to evaluate the biocompatibility of these biomaterials in vivo, as illustrated in Figure 1.

#### 2. Results

# 2.1. Synthesis and Chemical Characterization of ELP-GelMA Hydrogel and Electrospun Scaffolds

To engineer ELP-GelMA hybrid composite scaffolds, GelMA was synthesized by adding methacrylic anhydride to a cold water fish-derived gelatin solution, which was selected for its higher solubility at 4 °C (required for ELP dissolution) compared with that of porcine-derived gelatin (Figure 2a). The selected ELP sequence was designed to enhance elasticity and structural stability by incorporating cysteine residues with thiol (-SH) moieties at both ends, enabling efficient photo-crosslinking (Figure 2b). To prepare the ELP-GelMA prepolymer, different concentrations of GelMA (3-10% weight/volume (w/v) and ELP (0-7% w/v) were dissolved in 1,1,1,3,3,3-hexafluoro-2-propanal (HFIP) at 20–25 °C. Fibrous mats were fabricated via electrospinning onto an aluminum collector, followed by photo-crosslinking using 1% w/v Irgacure 2959 and 600 s of UV exposure. Upon UV irradiation, methacrylate moieties in the GelMA prepolymer reacted with the -SH groups of the ELPs (Michael addition), disulfide (-S-S-) bonds formed between the ELP chains, and C—C bonds formed within the GelMA chains (Figure 2c). The insolubility of the crosslinked scaffolds in aqueous solutions confirmed their crosslinking efficiency. Proton nuclear magnetic resonance (1H NMR) spectra of uncrosslinked prepolymers revealed peaks corresponding to methacrylate and methacrylamide groups at approximately 5.3 and 5.7 ppm, respectively (labeled as b and c in Figure 2d).

onlinelibrary.wiley.com/doi/10.1002/adhm.202500651 by University Of California, Los Angeles, Wiley Online Library on [22/08/2025]. See the Terms

onditions) on Wiley Online Library for rules of use; OA articles are governed by the applicable Creative Commons

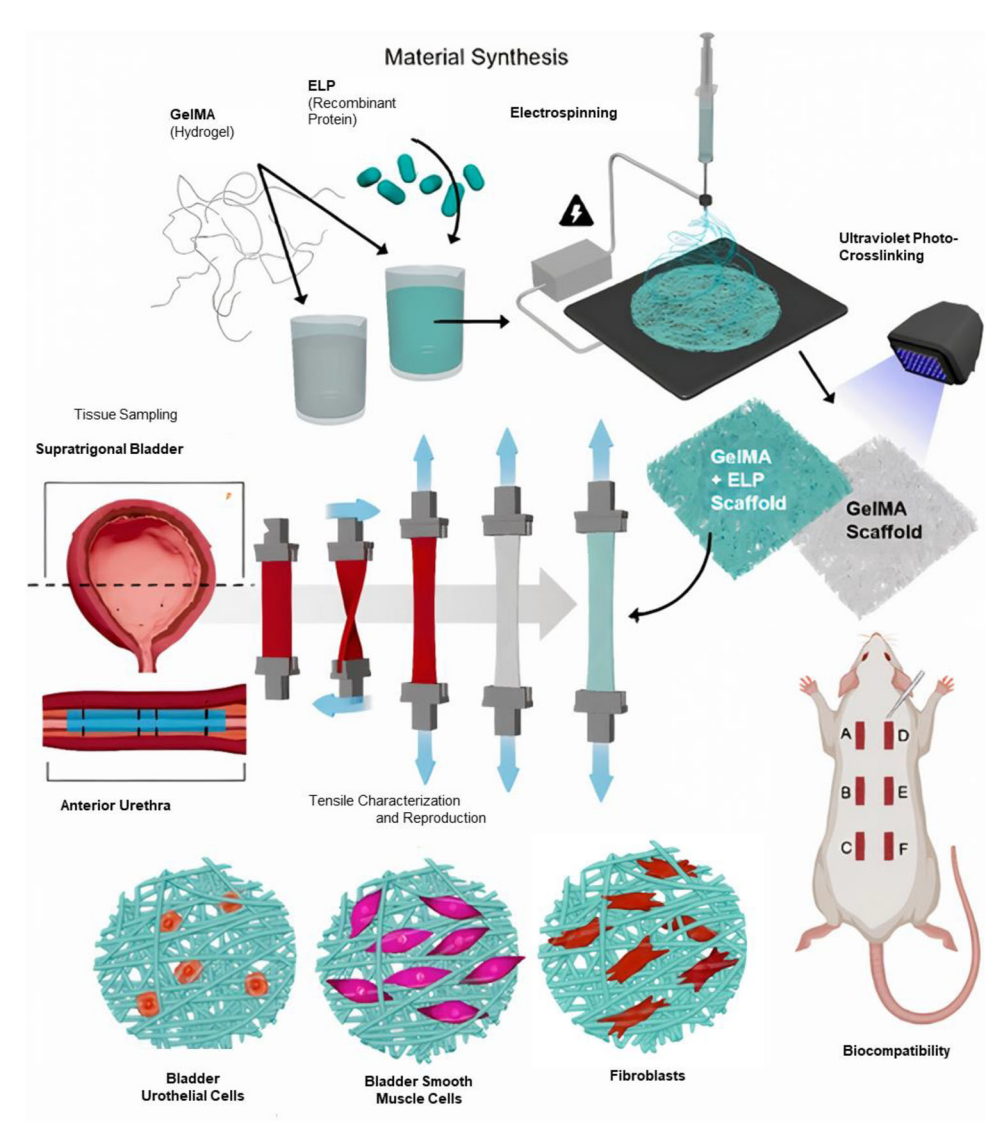


Figure 1. Schematic representation of the synthesis and evaluation of elastin-like peptide (ELP)—gelatin methacryloyl (GelMA) fibrous scaffolds. The process includes electrospinning of ELP—GelMA fibers, photo-crosslinking, mechanical characterization, in vitro cell seeding, and in vivo biocompatibility assessment via subcutaneous implantation in a rat model.

Representative scanning electron microscopy (SEM) images of the 5E5G and 0E10G scaffolds demonstrated highly porous fibrous structures (Figure 2e,f). The fiber diameters in 5E5G scaffolds (0.79  $\pm$  0.04  $\mu m$ ) were significantly smaller than those in 0E10G scaffolds (1.26  $\pm$  0.05  $\mu m;$  p < 0.01; Figure 2g). However, there was no significant difference in porosity between 0E10G (21.00%  $\pm$  0.17%) and 5E5G (18.91%  $\pm$  1.35%) (Figure 2h).

## 2.2. Mechanical Characterization of ELP-GelMA Scaffolds Compared with LUT Tissue and Commercial dECM

Given the critical role of scaffold biomechanical properties as critical regulators of cell phenotype, the mechanical properties of hydrogels containing different concentrations of GelMA (i.e., 3%, 5%, 7%, and 10% w/v) and ELP (i.e., 0%, 3%, 5%, and 7% w/v) were investigated and compared with those of native LUT tis-

sues and commercial ECM. LUT tissue samples were obtained from healthy young adult male New Zealand White rabbits (4–5 months old). Samples were collected immediately after euthanasia from the anterior urethra and supratrigonal bladder for tensile characterization (n = 7 per site).

In uniaxial tensile testing, the urethral tensile modulus (TM) was  $58.89 \pm 16.54$  kPa, showing no significant difference from that of the bladder (153.6  $\pm$  46.87 kPa; p > 0.05) (Figure 3a). Similarly, the ultimate tensile strength (UTS) did not differ between the two sites (urethra:  $99.82 \pm 24.14$ ; bladder:  $138.85 \pm 40.56$  kPa) (Figure 3b). Urethral samples also exhibited no significant difference in extensibility (%E) (322.59%  $\pm$  71.51%) compared with that of bladder tissue (194.54%  $\pm$  21.35%) (Figure 3c).

Next, the mechanical properties of hydrogels containing different concentrations of ELP and GelMA were evaluated. In uniaxial testing across all concentrations, the scaffolds exhibited a TM ranging from 12.44  $\pm$  2.08 to 25.63  $\pm$  4.77 kPa, with no signifi-

onlinelibrary.wiley.com/doi/10.1002/adhm.202500651 by University Of California, Los Angeles, Wiley Online Library on [22/08/2025]. See the Terms and Conditions

onditions) on Wiley Online Library for rules of use; OA articles are governed by the applicable Creative Comn

www.advancedsciencenews.com

www.advhealthmat.de

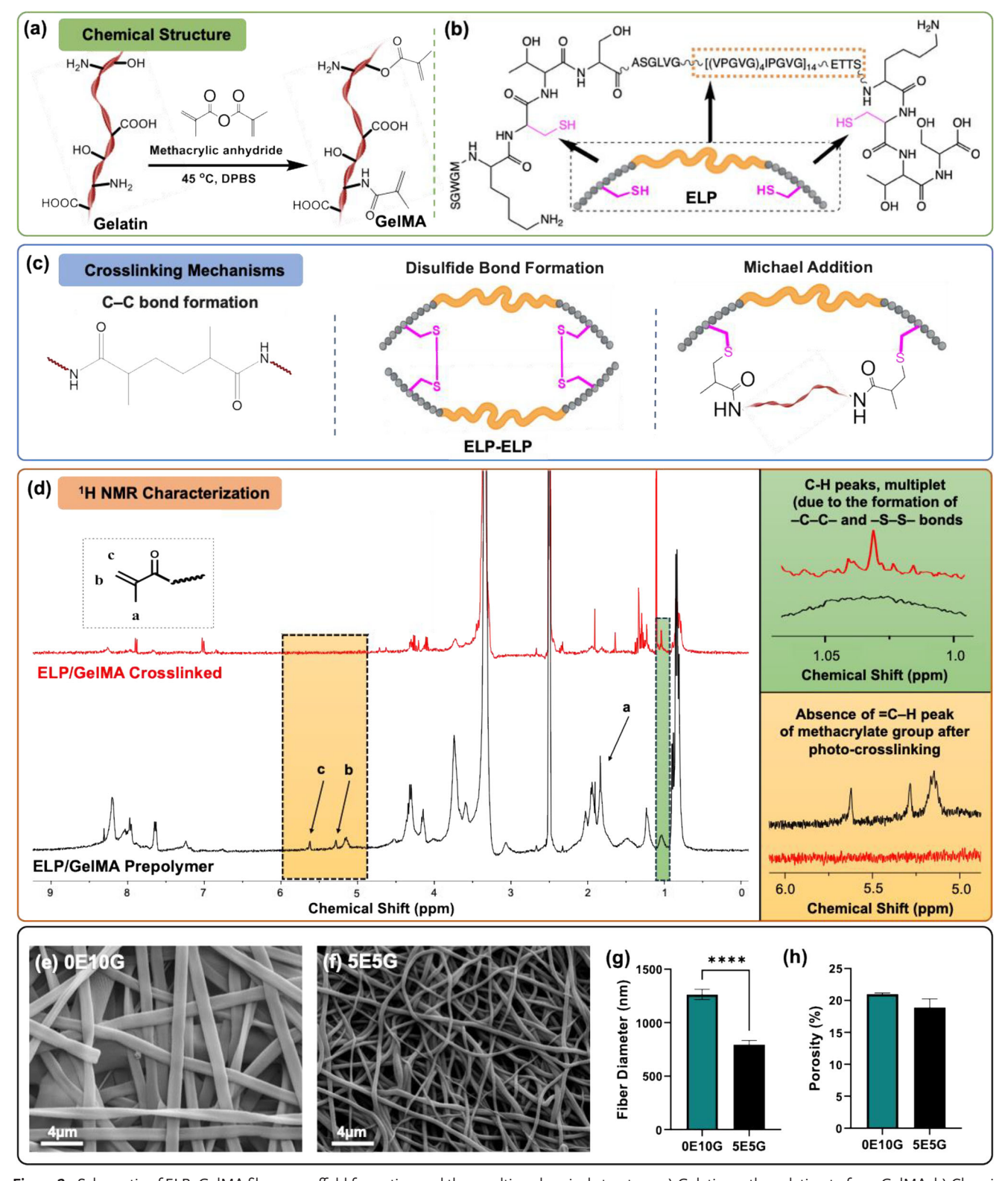
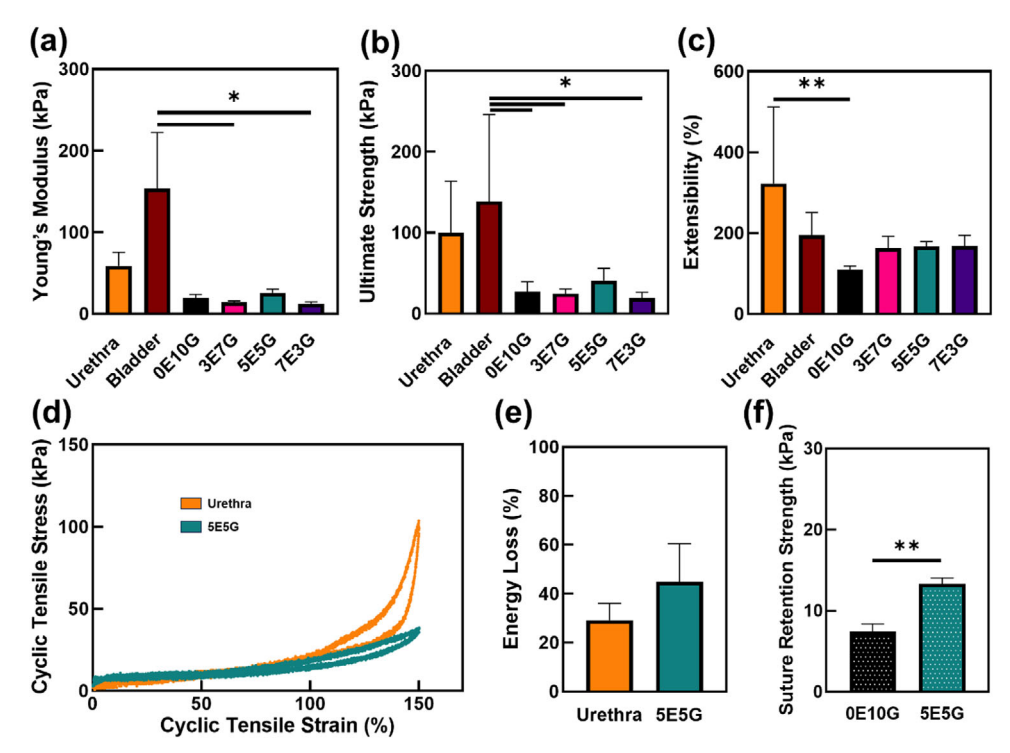


Figure 2. Schematic of ELP–GelMA fibrous scaffold formation and the resulting chemical structure. a) Gelatin methacrylation to form GelMA. b) Chemical structure of the customized ELP, indicating the presence of a thiol group. c) Crosslinking mechanisms involved in the ELP–GelMA hydrogel formation. d) Proton nuclear magnetic resonance (<sup>1</sup>H NMR) characterization, confirming the presence of methacrylated groups in ELP/GelMA prepolymer and successful crosslinking. e,f) Representative scanning electron microscopy (SEM)images of electrospun 0E10G and 5E5G scaffolds. g) Fiber diameter and h) porosity assessments of resulting scaffolds.

onlinelibrary.wiley.com/doi/10.1002/adhm.202500651 by University Of California, Los Angeles, Wiley Online Library on [22/08/2025]. See the Terms and Conditions (https://onlinelibrary.wiley.com/term

and-conditions) on Wiley Online Library for rules of use; OA articles are governed by the applicable Creative Commons License

www.advhealthmat.de



**Figure 3.** Mechanical properties and suture retention of photo-crosslinkable fibrous GelMA (n = 5) and ELP–GelMA (n = 5) scaffolds compared with those of adult male New Zealand White rabbit anterior urethral and bladder tissues (n = 7). a) Tensile modulus, b) ultimate tensile strength, and c) extensibility. d) Representative eighth cyclic tensile curves and energy loss of urethral tissue (n = 8) versus 5E5G candidate scaffolds (n = 4). f) Ultimate suture retention strength of scaffold-to-tissue configurations. p-Values were determined by ANOVA followed by Tukey's post hoc test for multiple group comparisons, and an unpaired two-tailed Student's t-test was used for two-group comparisons: p = 0.05, p = 0.01.

cant difference from the TM values of the bladder or urethral tissues, regardless of polymer concentration (Figure 3a). However, 5E5G scaffolds, with a TM of 25.63  $\pm$  4.77 kPa, were most readily handled by surgeons during a qualitative evaluation of tissue-like qualities for suture placement.

The UTS of the engineered hydrogels ranged from 19.43  $\pm$  3.08 to 27.48  $\pm$  5.32 kPa, with no significant difference observed across polymer concentrations or compared with bladder tissue. However, among the polymer concentrations, the UTS of 5E5G (40.96  $\pm$  6.68 kPa) did not significantly differ from urethral (99.82  $\pm$  24.14 kPa) and bladder tissues (138.85  $\pm$  40.56 kPa) (Figure 3b).

While 0E10G demonstrated a significant difference in %E compared with the urethra (109.13%  $\pm$  4.39%; p < 0.01), this difference was not observed in scaffolds containing ELP, which exhibited %E values ranging from 162.87%  $\pm$  13.2% to 168.25%  $\pm$  11.77% (Figure 3c).

Taken together, the addition of ELP improved both the quantitative and qualitative handling properties of the hybrid scaffolds, enhancing their approximation of the native LUT tissue. Based on these results, 5E5G was selected as the primary candidate material, with 0E10G serving as a second, well-characterized biomaterial for subsequent in vitro and in vivo testing.

Uniaxial tensile evaluation of small intestinal submucosa (SIS) (Lots: G13221, C-SLH-1S-2  $\times$  3, G12581, and C-SLH-1S-7  $\times$  10) demonstrated a TM of 16 041.64  $\pm$  1890.92 kPa (p < 0.0001) and %E of 67.83%  $\pm$  5.61% (p < 0.01), signifying that SIS is a stiffer and less extensible substrate than LUT tissue (Figure S1, Supporting Information).

Cyclic testing evaluated ten cycles of extension and relaxation of anterior urethral tissue (n=8) versus the 5E5G scaffold material (n=4). The eighth cycle is shown as a representative curve, with substantial overlap observed between 5E5G and the urethra, representative of cycles 2–10 (Figure 3d). The calculated energy loss for urethral tissue in cycle 8 was 29.09%  $\pm$  6.95% (Figure 3e). Cyclic tensile testing of 5E5G scaffolds demonstrated an energy loss of 44.86%  $\pm$  15.63%, with no significant difference from that of urethral tissue (Figure 3e). Specifically, the combined low energy dissipation and high resilience of the 5E5G hydrogels during loading and unloading cycles underscores their applicability for dynamic organ systems such as the bladder or urethra.

In addition, the suturability of ELP–GelMA fibrous scaffolds was assessed (n=3–4). The incorporation of ELP into the hydrogel network qualitatively improved hydrogel handling during the suture test. When evaluating scaffold-to-tissue suturing under conditions consistent with anticipated use, a significant increase was observed ( $7.41 \pm 0.97$  kPa, 0E10G vs  $13.29 \pm 0.75$  kPa, 5E5G; p < 0.01) (Figure 3f). Overall, these results demonstrate that suturability and suture retention can be achieved and enhanced by combining GelMA and ELP in electrospun scaffolds.

## 2.3. Enzymatic Degradation and Swelling Ratio Analysis of Electrospun Scaffolds

The enzymatic degradation and water uptake capacity of the ELP–GelMA fibrous hydrogels were evaluated to ensure scaffold stabil-

21922596, 0, Downloaded from https://advaced.onlinelibrary.wiley.com/ob/10.1002/athm.20200051 by University Of California, Los Angeles, Wiley Online Library on [22082025]. See the Terms and Conditions (https://onlinelibrary.wiley.com/errens-and-conditions) on Wiley Online Library for rules of use; OA articles are governed by the applicable Centitive Commons I

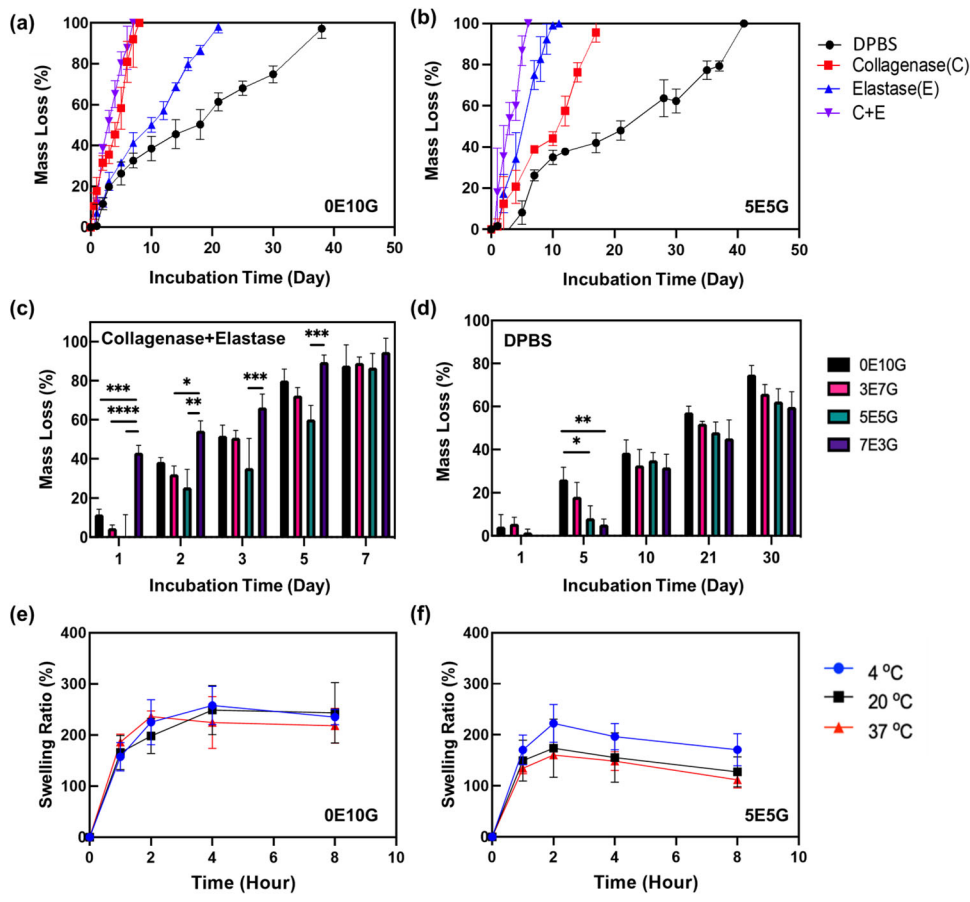


Figure 4. Biodegradation and swelling behavior of ELP–GelMA scaffolds. Degradation profile for a) 0E10G (n=3) and (b) 5E5G (n=3) scaffolds in DPBS, collagenase, elastase, and combined enzymes. Comparisons of the degradation profiles of various compositions of ELP–GelMA scaffolds (n=3) (0E10G, 3E7G, 5E5G, and 7E3G) at selected time points in c) combined collagenase and elastase, and d) DPBS. Swelling ratios of e) 0E10G (n=3) and f) 5E5G (n=3) scaffolds at 4, 20, and 37 °C. p-Values were determined by ANOVA followed by Tukey's post hoc test for multiple group comparisons, and an unpaired two-tailed Student's t-test was used for two-group comparisons: p < 0.05, p < 0.01, p < 0.001, p < 0.0001.

ity. To assess the differential effects of proteolytic enzymes on the scaffold chemical composition, the scaffold degradation rates of varied concentrations of ELP-GelMA (0E10G, 3E7G, 5E5G, and 7E3G) were characterized at 37 °C until complete degradation (Figure 4a,b). Samples were evaluated in triplicate for degradation and swelling at each time point. Two enzymes, elastase and collagenase, targeted the ELP and GelMA biomaterial components, respectively. Supraphysiological concentrations of the selected proteolytic enzymes enhanced their effects on the biomaterial degradation patterns; specifically, collagenase was particularly effective in degrading GelMA, whereas elastase increased the degradation rates of ELP-containing scaffolds. For example, the collagenase solution resulted in >50% degradation of 0E10G by day 5, compared with >50% degradation of 5E5G by day 12 (Figure 4a,b). In contrast, the elastase solution caused >50% degradation of 0E10G by day 10, versus day 7 for 5E5G. Combining the two enzymes further accelerated degradation, with >50% degradation observed across evaluated ELP compositions by day 3 (Figure 4c).

In addition to the evaluation in the presence of enzymes, the weight loss of scaffolds with varying compositions (0E10G, 3E7G, 5E5G, and 7E3G) was assessed in a Dulbecco's Phosphate

Buffered Saline (DPBS) solution to verify their relative stability following use in a surgical environment. The results revealed the role of ELP in reducing early degradation, followed by the overall stabilization of the scaffold weight loss from day 10 onward across all compositions (Figure 4d). All scaffolds were completely degraded in DPBS between days 38 and 45.

Both 0E10G and 5E5G scaffolds exhibited rapid swelling within 1 hour of incubation, regardless of temperature. However, no further significant swelling was observed after 4 hours of incubation (Figure 4e,f). In addition, the 5E5G scaffolds demonstrated overall lower swelling ratio than the 0E10G scaffolds. Furthermore, no significant difference in the swelling ratio of the 0E10G scaffolds was observed across the different incubation temperatures, whereas the 5E5G scaffolds showed significantly higher swelling ratio at 4  $^{\circ}$ C compared with higher temperatures.

### 2.4. In-Vitro Cytocompatibility Analysis of ELP-GelMA Fibrous Scaffolds

To assess the cytocompatibility of the candidate scaffolds, cell adhesion, proliferation, metabolic activity (n = 4 in

onlinelibrary.wiley.com/doi/10.1002/adhm.202500651 by University Of California, Los Angeles, Wiley Online Library on [22/08/2025]. See the Terms and Conditions

and-conditions) on Wiley Online Library for rules of use; OA articles are governed by the applicable Creative Commons



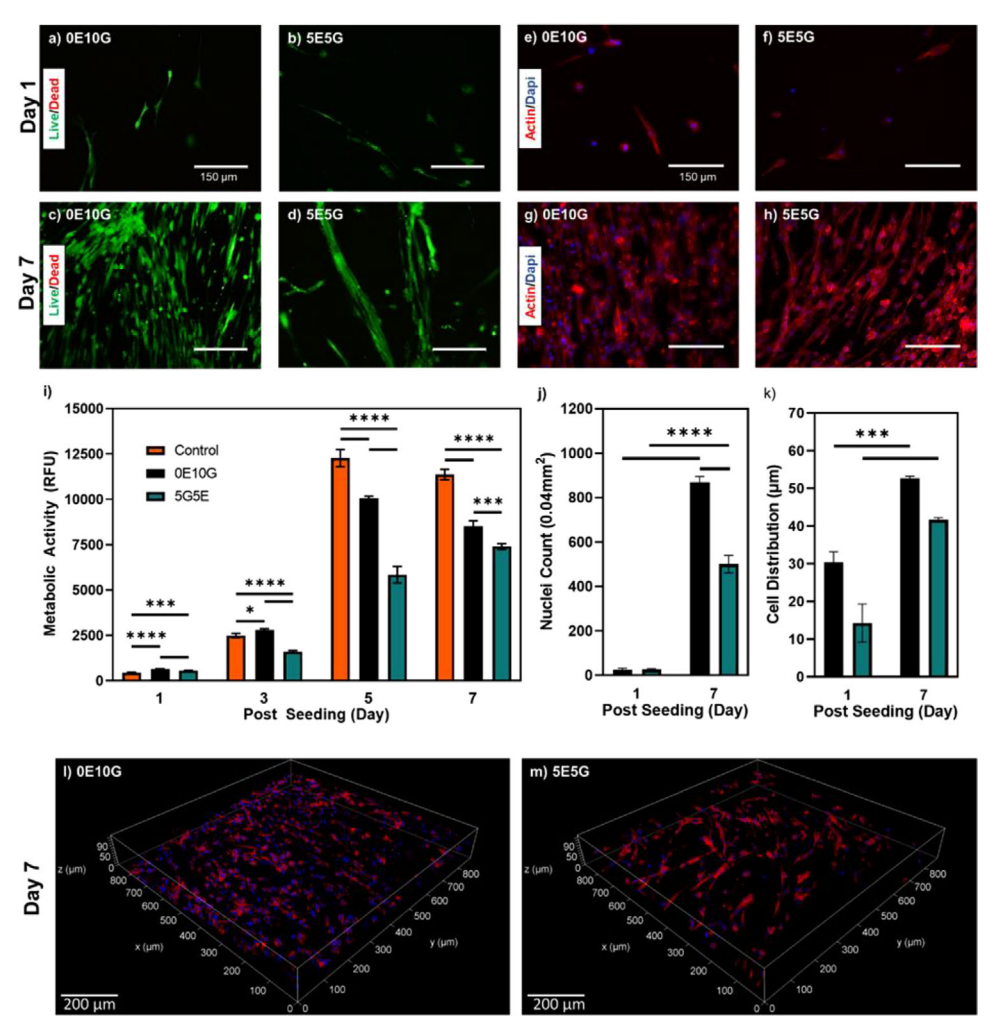


Figure 5. In vitro cytocompatibility study of human bladder smooth muscle cells on fibrous scaffolds over days 1–7. a–d) Representative stained images; e–h) representative Actin–DAPI immunohistochemistry (IHC) images at 20× magnification; i) quantitative cell viability analysis using PrestoBlue, reported in relative fluorescence units (RFU) (n = 4); j) quantitative cell proliferation analysis (n = 4); k) quantitative assessment of the cell distribution within the scaffold (n = 9); and l, m) representative day 7 Actin–DAPI IHC confocal isometric projections at 10× magnification. p-Values were determined by ANOVA followed by Tukey's post hoc test for multiple group comparisons, and an unpaired two-tailed Student's t-test was used for two-group comparisons: p < 0.05, \*\*\*p < 0.001, \*\*\*\*p < 0.0001.

quadruplicate per endpoint), and 3D distribution (n=9 tiles per condition) were evaluated. Cell lines relevant to the LUT, including human bladder-derived smooth muscle cells (SMCs), bladder-derived urothelial cells (UCs), and neonatal preputial fibroblasts (Fibs), were seeded onto 0E10G and 5E5G scaffolds under monoculture conditions. Both scaffolds were found to be cytocompatible, with live—dead assays demonstrating >98% mean cell survival at days 1 to 7 for all three cell lines (**Figure 5a**–d; Figures S2a–d and S3a–d, Supporting Information).

However, proliferation varied among the cell lines. Specifically, SMC nuclei counts, based on DAPI staining, increased rapidly (>10-fold over 7 days) on both 5E5G (day 1: 26.2  $\pm$  4.24 cells per 0.04 mm²; day 7: 500.4  $\pm$  39.27; p < 0.001) and 0E10G (day 1: 25.6  $\pm$  6.87; day 7: 868.8  $\pm$  25.65; p < 0.0001) scaffolds (Figure 5e–h,j). Similarly, Fib nuclei counts increased on both 5E5G (day 1: 19.75  $\pm$  2.46; day 7: 246  $\pm$  20) and 0E10G (day 1: 20.5  $\pm$  1.85; day 7: 245  $\pm$  32.42) scaffolds (Figure S3e–h,j). Supporting Information).

In contrast, UCs demonstrated a pattern of selective migration to the base of each well, with decreasing UC nuclei counts observed on both 5E5G (day 1: 52.75  $\pm$  6.02 cells per 0.04 mm²; day 7: 13.5  $\pm$  5.01; p < 0.01) and 0E10G (day 1: 48.25  $\pm$  5.89; day 7: 6.5  $\pm$  1.26; p < 0.01) scaffolds (Figure S2e–h,j, Supporting Information). Despite these differences in nuclear counts, all three cell lines demonstrated increased metabolic activity from days 1 to 7 on both the 0E10G and 5E5G scaffolds (p < 0.05) (Figure 5i; Figures S2i and S3I, Supporting Information).

Finally, cell distribution and spreading were visualized using confocal imaging of cytoskeletons and nuclei stained with actin and DAPI, as shown in Figure 5k–m at 20× magnification. For both the 5E5G and 0E10G scaffold compositions, the SMC and UC cell distributions increased from days 1 to 7 (SMC: p < 0.001; UC: p < 0.01) (Figure 5k–m; Figure S2k–m, Supporting Information). However, the Fib cell distribution increased between days 1 and 7 on the 5E5G scaffold (p < 0.0001), whereas a decrease



www.advhealthmat.de

was observed on the 0E10G scaffold over the same period (p < 0.0001) (Figure S3k-m, Supporting Information).

In summary, both the 0E10G and 5E5G scaffolds supported sustained cell metabolic activity over a 7 day period, with robust proliferation and cell adhesion in the SMC and Fib cohorts. While UCs adhered to the scaffolds, their proliferation was limited compared with that of the SMC and Fib cell lines. These findings warrant further investigation into scaffold modifications aimed at enhancing cell adhesion and propagation in cell lines.

### 2.5. In-Vivo Subcutaneous Implantation of ELP-GelMA and Commercial SIS in Rats

Biomaterials must not only promote cell propagation in vitro but also demonstrate clinical translatability, necessitating in vivo evaluation of scaffold degradation and foreign body responses, including local tissue regeneration and immune responses. To this end, in vivo biocompatibility testing was completed by comparing outcomes following implantation of the 5E5G and 0E10G candidate scaffolds, SIS, and sham wound creation.

#### 2.5.1. Anatomic Findings at Surgical Endpoint

To complete in vivo biocompatibility testing, healthy male rats were evaluated at days 1, 7, 14, 28, and 56, with a total of 40 animals included (n = 2 animals with 12 total subcutaneous sampling sites per endpoint and condition). On postoperative day 1, the 0E10G, 5E5G, and SIS implants remained in subcutaneous positions without gross degradation and could be readily removed without tissue dissection (Figure 6a). By week 1, the 0E10G and 5E5G scaffolds remained visible but decreased in size, whereas the SIS scaffolds remained unchanged. At week 2, both 0E10G and 5E5G showed partial integration with the surrounding tissue, requiring tissue dissection for removal. In contrast, SIS demonstrated inconsistent tissue integration and limited gross degradation. At 1 month postoperatively, the 0E10G and 5E5G scaffolds were further degraded but still visible, with ongoing tissue ingrowth into each construct. By 2 months, the 0E10G and 5E5G cohorts demonstrated complete gross degradation, with no visible scaffold material remaining and no apparent differences compared with the sham cohorts. In contrast, the SIS scaffolds, although partially degraded, remained palpable and visible, with clear evidence of local tissue ingrowth (Figure 6a). No visible fibrotic capsules were observed upon gross dissection in any cohort. Across all groups, animals remained in excellent clinical condition, with no postoperative infections, wound complications, or mortality observed from day 1 through the 2 month post-implantation endpoint.

#### 2.5.2. Analysis of Tissue Adjacent to Biomaterial Implantation

Histological analysis of tissues adjacent to the 0E10G, 5E5G, and SIS implants was performed at each endpoint and compared with the findings from sham surgery. For each condition and time point, two tissue samples (from different pockets) were collected per rat. Overall, the microscopic observations were consistent

with the gross pathology (Figure 6b; Figure S4a, Supporting Information). On day 1, all implants were visible and clearly distinct from the surrounding tissue, with no evidence of inflammatory infiltration. By week one, early tissue ingrowth was observed in the 0E10G and 5E5G scaffolds, whereas the SIS scaffold remained positioned between the tissue layers. At week 2, increased tissue regeneration was evident, accompanied by less distinct borders in the 0E10G and 5E5G scaffolds. After 1 month, the SIS scaffold remained visible with partial tissue ingrowth, whereas the 0E10G and 5E5G scaffolds were indistinguishable from the regenerated tissue. By 2 months, none of the three implants could be histologically differentiated from the surrounding tissue. In addition, no fibrotic capsules were histologically identified in any of the experimental cohorts.

To further evaluate the local immune cell response, immunohistochemistry (IHC) staining was performed for CD68 (macrophage), myeloperoxidase (MPO, neutrophil), and CD3 (Tcell) antigen markers adjacent to the implants and compared with sham controls. Rats implanted with SIS exhibited elevated early marker counts compared with those of the sham tissues (CD68 day 7, p < 0.01; MPO day 1, p < 0.05 and day 7, p = 0.001). A late inflammatory response was also evident, with increased CD3 levels in the SIS versus sham cohorts on day 56 (p < 0.01). Only CD68 at day 28 demonstrated a decrease in SIS compared with that of the sham cohorts (p < 0.05), while all other time points showed no significant differences. In contrast, all early and late immune marker counts in both the 0E10G and 5E5G cohorts remained stable or significantly decreased compared with the sham values. Specifically, 0E10G showed a significant decrease compared with the sham cohorts at four endpoints (CD68 day 28, p < 0.01; MPO day 56, < 0.001; CD3 day 1, < 0.001 and day 28, < 0.05), while 5E5G demonstrated a decrease at six endpoints (CD68 day 1, < 0.05; MPO days 1 and 56, < 0.001; CD3: day 1, < 0.001, day 7, < 0.05, and day 28, < 0.001) relative to the sham values (Figure 6c; Figure S4b, Supporting Information). Overall, both the 0E10G and 5E5G cohorts demonstrated excellent biocompatibility throughout the scaffold degradation and regenerative periods, with no increases in macrophage, neutrophil, or T-cell immune markers at any time point.

#### 3. Discussion

A clinical challenge in LUT tissue engineering is the development of biomaterials with mechanical properties that accurately replicate the tensile characteristics of native LUT tissues. Although gelatin-based hydrogels are inherently biomimetic, their limited tensile strength and extensibility have hindered their clinical translation for use in distensible organs such as the bladder and urethra. To address this limitation, we leveraged genetically encoded synthesis of ELPs, enabling precise control over the amino acid sequences and physicochemical properties. This tunability makes ELPs particularly well-suited for biomedical applications requiring high extensibility. Based on this, we hypothesized that incorporating ELPs into GelMA-based hydrogels would enhance their TM, %E, and suturability upon photocrosslinking, ultimately yielding constructs with biomechanical properties closely resembling those of healthy LUT tissues.

Urethral and bladder tissues possess tensile properties essential to their physiological function, enabling repeated distension

21922659, 0, Downloaded from https://advanced.

onlinelibrary.wiley.com/doi/10.1002/adhm.202500651 by University Of California, Los Angeles, Wiley Online Library on [22/08/2025]. See the Terms and Conditions

nd-conditions) on Wiley Online Library for rules of use; OA articles are governed by the applicable Creative Commons I

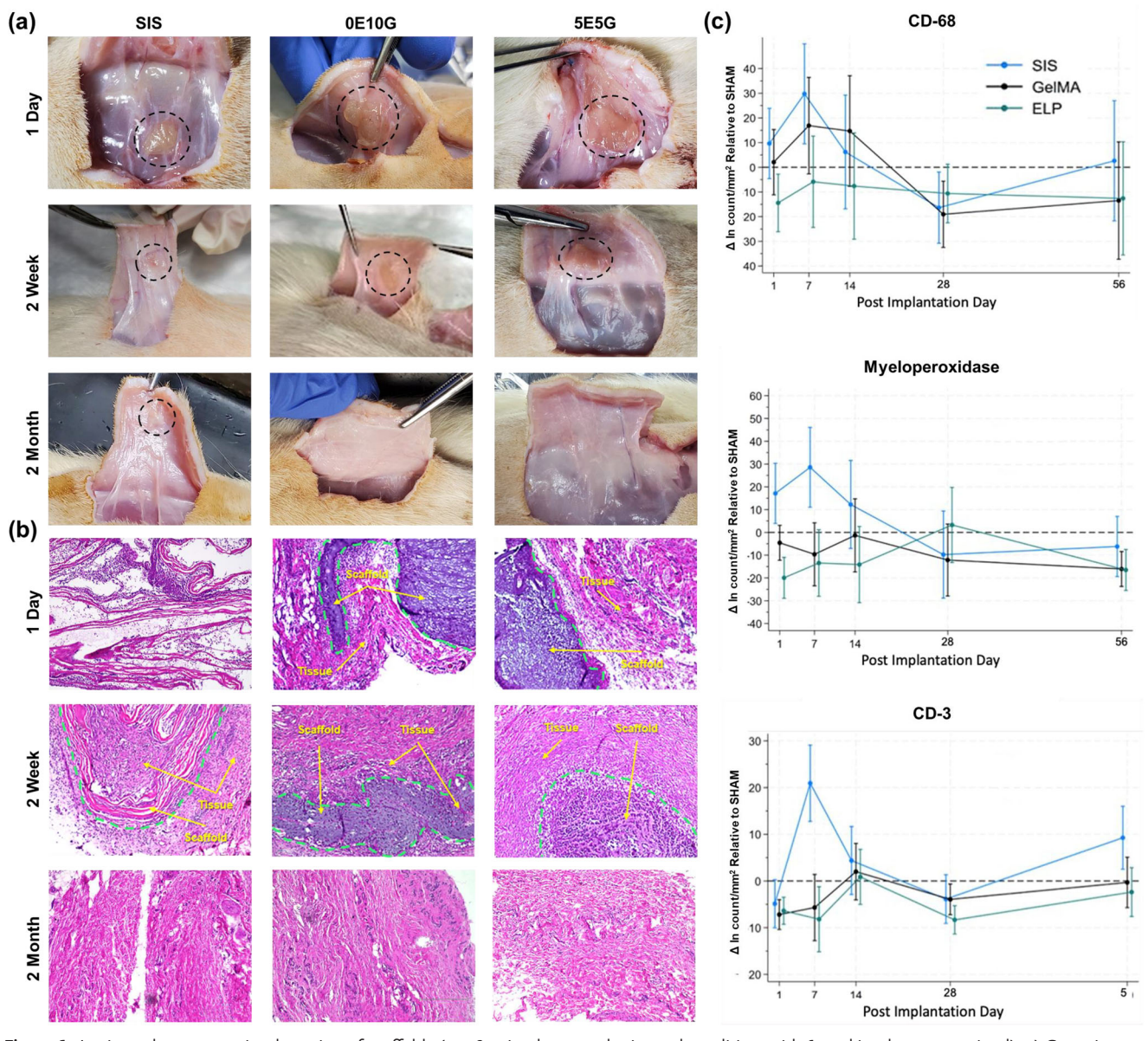


**Figure 6.** In vivo subcutaneous implantation of scaffolds (n = 2 animals per endpoint and condition, with 6 total implants per animal). a) Gross images of implanted scaffolds, b) hematoxylin-and-eosin staining of tissues at the implantation site, and c) quantification of IHC markers illustrating mean and standard error for each data point, with zero representing the sham value.

and recoil during thousands of voiding cycles over a lifetime. The resultant candidate 5E5G scaffolds demonstrated no significant differences in modulus, strength, or elasticity compared with those of healthy LUT tissue. Furthermore, 5E5G exhibited a low energy loss across multiple loading and unloading cycles, which is critical for restoring voiding function and minimizing the risk of urinary leaks under repetitive mechanical stress. In summary, the proposed 5E5G scaffold was designed to replicate the tensile properties of native LUT tissue.

While prior biological and synthetic scaffolds have been developed to mimic the structural properties of the LUT ECM, comparatively less attention has been given to replicating the tensile properties of the bladder and urethra. [25] For example, the current study highlights a >100-fold difference in the TM between a com-

mercially available dECM product, SIS, and native LUT tissue. In addition, although biomaterials have successfully supported UC and SMC regeneration in pre-clinical models, their clinical application has been limited by issues such as poor physiological function, graft contracture, and fibrosis. [26] A recent study addressed this challenge by modifying dECM with long aliphatic chains to better emulate bladder extensibility and modulate scaffold degradation. [27] Compared with dECM controls, the modified dECM increased pro-regenerative macrophage infiltration and enhanced bladder wall regeneration in a pre-clinical bladder augmentation model. [27] Similarly, a recent study on synthetic materials illustrated that microgrooved poly(1, 8, octamethylenecitrate-co-octanol) scaffolds, designed to replicate native tissue to-pography and tensile properties, improved UC regeneration and



www.advhealthmat.de

microvasculature formation.<sup>[28]</sup> Collectively, these results indicate that both the structural and tensile properties are critical to effective LUT tissue regeneration and function. This study represents a timely advancement in the development of a tunable biomaterial guided by these design criteria.

However, the proposed scaffolds are promising not only because of their tunable tensile properties but also due to the versatility of their fabrication method. A key aspect of electrospinning is its versatility, which enables the creation of multi-layered microenvironments, with the characteristics of each microenvironment tailored to the primary cell line. [29] This customization can be achieved through adjustments in crosslinking parameters, material ratios, and spinning techniques (e.g., generating aligned fibers using a mandrel to enhance smooth muscle contractility). Such approaches provide reproducible modifications across multiple scaffold dimensions, including the presence of cell-binding sites, nanotopography, swelling behavior, and degradation kinetics.<sup>[30]</sup> Furthermore, selecting materials with functional groups, such as the modifiable peptide repeat sequence in ELPs and the RGD domain in gelatin, enables a range of biologically active modifications that can improve vascularization, wound healing, and immunomodulation.[31] Starting with materials that allow for structural, mechanical, and bioactive customization tailored to each target organ and translational goal can facilitate tissue matching across diverse clinical applications, patient demographics, and surgical conditions.

In addition, the swelling and degradation behavior of the constructs are critical considerations, as higher swelling rates of implanted scaffolds can result in significant morphological changes,[32] thereby affecting flow patterns and luminal dimensions in fluid-filled structures. In addition, for clinical applications, it is imperative that the engineered polymeric networks degrade into nontoxic byproducts, while supporting autologous cell proliferation and tissue regeneration.[33] Overall, ELP-GelMA fibrous scaffolds exhibit tunable degradation and can remain stable in physiological environments for up to 1 month during in vitro seeding or implantation, thereby facilitating cell seeding and early ECM deposition necessary for remodeling and tissue regrowth. Furthermore, the swelling results showed that the 5E5G scaffolds exhibited lower swelling compared with that of the 0E10G scaffolds, which can be attributed to the hydrophobic repeating motifs (([VPGVG]<sub>4</sub>[IPGVG])<sub>14</sub>) within the ELP chemical structure that contribute to reduced swelling ratios. [22,34]

Despite being cytocompatible, scaffold materials support varying levels of cell growth and proliferation across different cell lines. Specifically, UCs demonstrated less cell proliferation on the scaffold materials but strong adherence and growth on the underlying well plate. Notably, tissue was evaluated to define the tensile target properties of a multi-layered intact urethra; however, prior studies using atomic force microscopy to evaluate the layers of the bladder wall have demonstrated that urethral and bladder tissues present differing microenvironments. [35] Thus, it is expected that UCs and SMCs may require distinct microenvironments to support optimal cell propagation. Furthermore, a balance must be maintained between cell-binding sites and increased elasticity, as this ratio may differ across cell lines, particularly for the epithelium, which establishes a multi-layered, watertight barrier essential for physiological function.<sup>[29]</sup> Current strategies to address the relatively low UC propagation include UC encapsulation versus seeding on a hydrogel layer alone, electrospinning with an increased fiber diameter, incorporating grooves into the fibers to enhance binding sites, or modifying the scaffold to increase the tensile strength of the UC layer. For SMCs, the next steps involve evaluating the effects of fiber alignment on the physiological contractile properties. Taken together, our engineered ELP–GelMA scaffolds developed for LUT establish a foundation for future multi-layered scaffolds that promote cell proliferation and functional ECM deposition, tailored to specific cell lines.

When implanted in an animal model, both the 0E10G and 5E5G scaffolds were replaced by subcutaneous tissue layers that appeared grossly and histologically normal. This was accompanied by complete scaffold degradation and a lack of fibrosis over a 2 month period. However, the commercial dECM product (SIS) induced a greater inflammatory response than the engineered scaffolds. Previous studies have reported variable immune responses to SIS samples, which may have contributed to these findings, [36] despite the use of multiple independent lots from the manufacturer in this study. The observed reductions in both early and late inflammation—most notably with the addition of ELP to GelMA across all endpoints—are consistent with previous findings that tropoelastin may promote a wound-healing immune phenotype and enhance neovascularization.[37] This is promising for its potential to enhance wound healing and warrants further investigation in both healthy and diseased LUT animal models.

The limitations of our study include those inherent to the development of a biomaterial with translational specifications derived from in vitro and animal models. For example, ensuring no significant difference in the selection of uniaxial and cyclic tensile parameters may provide an adequate approximation to support translatability across individuals, animals versus human models, and disease states. Future studies are planned to evaluate the effects of tensile properties on the cell phenotype and proliferation using additional immunofluorescent markers (e.g., pan-cytokeratin and its subtypes,  $\alpha$ -smooth muscle actin, and the proliferation marker Kiel Ki67). In addition, changes in proteomics and gene expression across different cell lines, as well as the impact of ECM deposition on tensile properties within various microenvironments-including static versus dynamic culture conditions (e.g., stretch-perfusion bioreactor application) represent critical next steps. Although in vivo testing in this study confirmed biocompatibility in a small animal model, functional analysis of the target organ system remains to be performed. Once multi-layered designs have been achieved in vitro, further evaluation of seeded and unseeded constructs is planned using a chronic urethral defect model of urethroplasty in rabbits, <sup>[29]</sup> allowing for the assessment of functionalization, innervation, and vascularization. In the future, this work will provide a framework for early mechanical and structural modifications, ensuring that biomaterial development techniques are guided from the outset by the intended translational requirements.

#### 4. Conclusion

Bladder and urethral tissues possess structural and functional parameters essential for lifelong voiding and penile tumescence. Biomimetic scaffolds that mimic the mechanical properties of the LUT were successfully engineered by electrospinning 5E5G,



www.advhealthmat.de

followed by photo-crosslinking. These scaffolds were suitable for application and exhibited a mean degradation of over 50% by day 21 in DPBS at 37 °C. Both 0E10G and 5E5G scaffolds exhibited excellent in vitro cytocompatibility, promoting the robust adhesion and proliferation of SMCs and Fibs, as well as the maintenance of UC cell lines. Upon implantation, both scaffolds reduced acute and chronic inflammation to levels at or below those observed in sham controls, with complete tissue degradation and regeneration in the absence of fibrosis at the 56 day endpoint. We anticipate that electrospun 5E5G scaffolds may provide an alternative tissue source for complex bladder and urethral repairs, offering suturability and the ability to recapitulate the structure and mechanics of native, healthy LUT tissues.

#### 5. Experimental Section

Surgical Excision of LUT Tissue from New Zealand White Rabbit Tissue: Bladder and penile tissues from male New Zealand White rabbits (18-20 weeks old) were collected as intact prosections immediately posteuthanasia through an institutional tissue-sharing program. Rabbits were selected because of their relevance as an established animal model for anterior urethroplasty and the similarity of their urethral tensile properties to those of humans.<sup>[29]</sup> Prior to LUT tissue extraction, animals had undergone a tracheal procedure followed by a 3 day course of dexamethasone 6 weeks before euthanasia (due to the tissue-sharing program). No additional medications were administered, and no effects on the LUT tissue were anticipated from the upper airway surgical procedure. For each section, the bladder was separated from the urethra at the bladder neck and opened with a vertical anterior incision to allow identification of the ureteral orifices. Supratrigonal bladder tissue samples were then collected. Subsequently, intact anterior urethral samples were excised from the underlying cavernosal bodies and divided dorsally to create longitudinal sheets for testing. All dissections were performed by a pediatric urologist using 2.5× loupe magnification.

GelMA Synthesis: GelMA synthesis has been previously described. [38,39] Briefly, cold-water fish skin gelatin (10 g) (Sigma-Aldrich) was dissolved in DPBS (100 mL) (Gibco), heated to 60 °C, and stirred until fully dissolved. Next, methacrylic anhydride (8 mL) (Sigma-Aldrich) was added dropwise to the gelatin solution while stirring (300 rpm) at 45 °C. The reaction was stopped after 3 hours by adding DPBS (300 mL, 40 °C), and the mixture was dialyzed (Spectrum Laboratories, MWCO = 12–14 kDa) against deionized water at 50 °C for 7 days to remove any unreacted methacrylic anhydride. Following sterile filtration, lyophilization continued for 5 days to generate a white porous foam, which was sterilely stored at 20–25 °C until electrospinning.

ELP Synthesis: A custom-designed ELP macromolecule was synthesized using genetically engineered kanamycin-resistant Escherichia coli containing 70 repetitive pentapeptide units, as previously described. [22] These repetitive pentapeptide units consisted of VPGVG amino acid residues, modified by substituting isoleucine for valine every fifth unit to yield the (([VPGVG]4[IPGVG])14) sequence. To enable photo-crosslinking through the formation of S–S thiol bonds, Lys–Cys–Thr–Ser (KCTS) residues were incorporated at both termini of the ELP sequence. Following synthesis, E. coli cells were lysed, and the ELP was purified using the inverse transition cycling method. [40] The resultant solution was dialyzed against deionized water at 4 °C for 7 days, then lyophilized. The resulting ELP was stored under sterile conditions until electrospinning.

Preparation, Electrospinning, and Crosslinking of the Prepolymer Solution: Selected weight percentages of GelMA by volume (3%, 5%, 7%, and 10%) with or without ELP (0%, 3%, 5%, and 7%) were dissolved in HFIP (Sigma-Aldrich). These prepolymer solutions were drawn into a syringe (1.5 mL) that was mounted onto a syringe pump affixed to a custom-made high-voltage electrospinning system (Glassman High Voltage, Inc., Series EH). 25 kV was applied to the needle, with an aluminum collecting plate (25 cm × 25 cm) positioned 13 cm from the syringe nozzle. The prepolymer so-

lution was extruded at a rate of 1 mL hour $^{-1}$ . Following fabrication, each fibrous scaffold was removed from the collection plate and placed in a desiccator overnight at 20–25 °C to remove any remaining solvent. The scaffolds were subsequently immersed for 2 hours in a 1% w/v solution of Irgacure 2959 (Sigma-Aldrich) photoinitiator in ethanol. Crosslinking was achieved by exposing each scaffold for 600 seconds to UV light (6.9 mW cm $^{-2}$ , EXFO OmniCure S2000), followed by a DPBS wash.

<sup>1</sup>H NMR Characterization of ELP–GelMA Scaffolds: Crosslinked and non-crosslinked fibrous scaffolds were characterized by <sup>1</sup>H NMR (400 MHz, Bruker AV400 spectrometer) using deuterated dimethyl sulfoxide (DMSO-d6, Cambridge Isotope Laboratories, Inc.) as the solvent. Fibrous scaffold samples (1 cm × 1 cm) were dissolved in DMSO-d6 (1 mL), and <sup>1</sup>H NMR spectra were recorded to verify polymer synthesis and determine crosslinking.<sup>[39]</sup> To assess hydrogel crosslinking, the spectra of the crosslinked ELP–GelMA hydrogel were compared with those of the ELP–GelMA prepolymer to ensure a significant reduction in the intensity of the methacrylate peaks, consistent with previous reports.<sup>[41]</sup>

Structural Analysis of Electrospun Scaffolds Using SEM: Each candidate scaffold sample was mounted on stubs and sputter-coated with gold using a sputter coater (SC7620; Quorum Technologies, UK). The structure of the electrospun scaffolds was characterized by SEM (ZEISS Supra 40VP scanning electron microscope) at 10 000× magnification and an accelerating voltage of 10 kV. Fiber diameters and pore sizes were measured using Image] software (National Institutes of Health, Bethesda, MD, US) applied to each SEM image. Fiber diameter was calculated as the mean of ten fibers measured per image, while the pore size was determined by measuring all pores in each of the same ten images.

Mechanical Characterization of LUT Tissues, Commercial Products, and Biomaterials: Hydrogel samples were prepared in rectangular PDMS molds (12 mm length  $\times$  6 mm width  $\times$  1.5 mm height) for tensile testing, as previously described.[42] Tissue samples of similar dimensions were also prepared, with the dimensions of both hydrogel and tissue samples measured using a caliper. Prior to testing, freshly resected tissue samples were maintained at 4 °C for a maximum of 24-48 hours. During testing, tissue samples were warmed to 20-25 °C and kept moist with DPBS throughout the evaluation. Tensile tests were conducted using an Instron 5542 mechanical tester. Samples were secured between two pieces of tape within the tension grips and extended at a rate of 1 mm minute<sup>-1</sup> until failure. The tensile stress and strain of each sample were recorded using Bluehill 3 software. The TM was calculated from the slope of the stressstrain curve within the strain range of 5-20%, whereas the UTS and %E were determined at the point of failure. Cyclic tensile tests (10 cycles per sample) were conducted with a maximum strain of 150% at a rate of 1.5% second<sup>-1</sup>.[42] The stress-strain curve from cycle 8 is presented as a representative example. The area between the loading and unloading curves during cycle 8 defined the energy loss.

Suture Retention Testing: Electrospun ELP-GelMA scaffolds were prepared as previously described. Rabbit urethral tissue and commercial samples were prepared for suture retention testing. Longitudinal anterior urethral tissue samples were prepared following established protocols, with all samples hydrated in DPBS prior to testing. A running single-layer approximation of tissue-to-scaffold or scaffold-to-scaffold (1 cm × 2 cm samples) was performed using a 5-0 monofilament suture (PDS II, J&J MedTech Ethicon) on an RB-2 needle by a pediatric urologist. The suture line included the full thickness of each sample (approximately 2-mm wide). Sutured samples were fixed between two pieces of double-sided tape within tension grips and extended at a constant rate of 1 mm minute<sup>-1</sup> using an Instron 5542 mechanical tester. The suture retention strength was defined as the maximum mechanical load (kPa) applied before the suture was pulled out from the respective material or tissue sample.

Enzymatic Degradation and Swelling Ratio Analysis: Circular samples of consistent size were obtained from the central portion of the candidate scaffolds using a 5-mm punch biopsy for degradation and swelling analyses. After a DPBS wash and lyophilization of each sample, the initial dry weight was recorded (W0). For degradation analysis, each sample was incubated at 37  $^{\circ}\text{C}$  in one of the following solutions until complete degradation: DPBS; a 0.1U mL $^{-1}$  porcine pancreas elastase solution



www.advhealthmat.de

(Millipore Sigma); a 1.5U mL<sup>-1</sup> type I collagenase solution (Sigma-Aldrich); or a solution composed of equal volumes of the 0.1U mL<sup>-1</sup> porcine elastase and 5U mL<sup>-1</sup> type I collagenase solutions in DPBS.<sup>[43]</sup> Specific to the LUT, elastase contributes to the degradation of elastin within the ECM in fibrotic and malignant bladder conditions,<sup>[44]</sup> while collagenase has been harnessed to treat fibrotic plaques in penile tissue and urethral stricture disease.<sup>[45]</sup> On days 1, 2, 4, 7, 10, 14, 21, and 28 (extended to days 30, 38, and 40, as needed), samples from each candidate material were retrieved, lyophilized, and weighed. The incubation solution was replaced every 3 days throughout the degradation period. The degradation rate (%) was calculated using the equation:

$$(W0 - W_t) (W0^{-1}) (100)$$
 (1)

where  $\it W0$  is the initial dry mass of each sample and  $\it W_t$  is the dry mass at each time point. $^{[46]}$ 

For swelling analyses, samples were immersed in DPBS at 4, 20–25 or, 37  $^{\circ}$ C for 1, 2, 4, and 8 hours until no further increase in the weight was observed. At each time point, a subset of samples was removed and immediately weighed. The swelling ratio (%) was calculated as:

$$(W_i - W0) (W0^{-1}) (100)$$
 (2)

where W0 is the initial dry mass of each sample and  $W_i$  is the mass at each time point.<sup>[47]</sup>

LUT Cell Line Selection, Verification, and Expansion for In Vitro Cytocompatibility Testing: Three commercial cell lines were used: human bladder SMCs (ATCC PCS-420-012), human bladder UCs (ATCC PCS-420-010), and human neonatal preputial foreskin Fibs (ATCC BJ CRL-2522). Each cell line was expanded under sterile conditions using cell line-specific media recommended by the manufacturer (ATCC) and maintained at 37 °C in a humidified atmosphere with 5% CO<sub>2</sub>.

Monoculture of LUT Cell Lines on Candidate Biomaterials: Prior to cell seeding, scaffolds were sterilized in 70% ethanol and exposed to germicidal UV light overnight. Scaffolds were then immersed in cell line-specific culture media at 37 °C for 48 hours prior to seeding, with a medium change after the first 24 hours. Once expanded (passages 2–5),  $10^4$  cells of each scaffold or SIS sample of each cell line were applied dropwise onto the surface of each candidate scaffold within 24-well plates containing 500  $\mu L$  of growth medium (ATCC PCS-100-030, PCS-100-042 for SMCs; ATCC PCS-420-032, PCS-420-042 for UCs; and ATCC 30–2003, 30–2020 for Fibs). After 1 hour, an additional 500  $\mu L$  of growth medium supplemented with penicillin–streptomycin (ATCC 30–2300) was added to each well. Cultures were maintained at 37 °C in a 5% CO2 humidified atmosphere, with media replaced every 48 hours.

Cell Viability Assay: The viability of SMC, UC, and Fib cell lines following seeding on fibrous scaffolds was determined using a commercial LIVE/DEAD  $^{TM}$  kit (Invitrogen). At days 1, 5, and 7, staining solution (50  $\mu L$  mL $^{-1}$ ) was added to each well, followed by incubation in the dark at 20–25 °C for 15 minutes prior to imaging. Fluorescent images were acquired using an Evos M5000 microscope at 4× and 20× magnifications (Invitrogen, Thermo Fisher). Images of cells stained with live–dead markers were captured at 10× magnification on an Evos 5000 (Thermo Fisher). Four paired representative images were taken for each cell type, scaffold type, and endpoint. For each pair of images (one red channel "dead" image and one green channel "live" image), the number of colored pixels was counted and summed using Image). The green pixels were divided by the total number of colored pixels to calculate the percentage of viable cells.

Metabolic Activity Assay: A commercial PrestoBlue assay (Life Technologies) was performed according to the manufacturer's instructions to assess the metabolic activity on days 1, 3, 5, and 7 post-seeding. At each time point, 10% PrestoBlue reagent was added to the media and incubated for 1 hour at 37 °C. Following a 1-h incubation at 20–25 °C, four aliquots of PrestoBlue containing solution (100  $\mu$ L) were collected from each well and transferred into separate wells of a 96-well plate. Fluorescence was measured using a Synergy HT fluorescence plate reader (BioTek) with excitation at 540 nm and emission at 600 nm. Wells containing only media and PrestoBlue served as blanks to establish background fluorescence.

RFU for each sample were calculated by subtracting the mean blank values from the experimental readings.

Assessment of Cell Adhesion, Proliferation, and Spreading on Candidate Biomaterials: To assess the cytocompatibility, one-ply SIS (Cook Biodesign) was selected as a commercial product for comparative analysis with the proposed scaffolds because of its FDA-approved indications for the reinforcement of soft tissues and prior clinical studies supporting its use in corporal body (penile) grafting and bladder neck support. [48] SIS has also been shown to be cytocompatible with LUT cell lines. [49] The presence of cells (nuclei) and cytoskeleton on the candidate scaffolds and SIS was visualized via IHC staining. Briefly, on days 1, 5, and 7 post-seeding, cells were fixed with 4% neutral buffered formalin (Epredia) for 15 minutes, rinsed with DPBS, and permeabilized with 0.1% Triton X-100 (Sigma-Aldrich) for 15 minutes. Following permeabilization and a subsequent DPBS rinse, 2 drops  $mL^{-1}$  of the ActinRed 555 ReadyProbes reagent (rhodamine phalloidin) (Thermo Fisher) were added to each well, and samples were incubated for 30 minutes at 20-25 °C. Subsequently, 2 drops mL<sup>-1</sup> of the NucBlue Fixed Cell ReadyProbes reagent (DAPI) (Thermo Fisher) were added to each sample, followed by an additional 30minutes incubation before IHC image capture. Confocal images (10x) were obtained on days 1 and 7 post-seeding for each candidate scaffold to evaluate the depth of cell penetration, spreading, and distribution throughout the fibrous 3D structure. Samples were stained for both F-actin and DAPI, embedded in 1% agar, and imaged using a TCS SPE high-resolution spectral confocal microscope (Leica). Images were processed with Lightning deconvolution software (Leica). The cellular distribution was analyzed by measuring the Z-position of each nucleus relative to the position of the most superficial nuclei on each scaffold.

Biocompatibility Surgical Procedure: The rat subcutaneous biocompatibility testing was performed under protocol ARC-2022-106 at UCLA. Adult Male Sprague-Dawley rats (10-12 weeks) were purchased from Charles River Laboratories Fach animal underwent either subcutaneous implantation or sham procedures, with the creation of six subcutaneous dorsal pockets per animal. Rats were assigned to each condition group—SIS, 0E10G, 5E5G, and sham—at defined endpoints of days 1, 7, 14, 28, and 56. Only males were used, reflecting the proposed use of these scaffolds in anterior urethroplasty (penile tissue). Perioperative pain control was achieved through oral administration of caprofen for 24-48 hours. Anesthesia was induced with 4% isoflurane and maintained at 2% throughout each procedure. Six vertical dorsal skin incisions, each 1-2 cm in length, were made. Subsequently, an ≈2-cm<sup>2</sup> lateral pocket was created by subcutaneous blunt dissection (2 incisions laterally  $\times$  3 incisions longitudinally). Each scaffold was inserted into a pocket, which was then closed using a staple. Rats designated as sham underwent the same procedure without scaffold implantation.

Sample Preparation for Implantation: 0E10G, 5E5G, and SIS samples (1 cm  $\times$  1 cm) were sterilized by immersion in 100% ethanol and exposure to UV light for 24 hours. Then, the samples were hydrated for 48 hours in DPBS, with the solution changed after 24 hours. Each well was inspected at 20 $\times$  and 40 $\times$  magnification for signs of contamination after 24 and 48 hours prior to implantation.

Surgical Sample Retrieval and Tissue Analyses: At the end of each time point, the rats were euthanized via  $\rm CO_2$  administration. Gross images were captured, and the scaffolds, along with surrounding tissues, were formalin-fixed, dehydrated, and embedded in paraffin. Sections that were 5–7-µm long were prepared as previously described, [50] followed by deparaffinization and rehydration. H&E staining (ab245880) was performed according to the manufacturer's instructions. For IHC staining, slides were blocked with 10% bovine serum (Thermo Fisher) for 30 minutes at 20–25 °C. Samples were then incubated with conjugated antibodies against MPO (0.2 µg mL $^{-1}$ ), CD-68 (0.2 µg mL $^{-1}$ ), and CD-3 (4 µg mL $^{-1}$ ) for 90 minutes at 20–25 °C, and subsequently mounted using toluene. All antibodies were sourced from SC Biotech. Central and distal images of each sample were obtained at 10× magnification using an EVOS M5000 microscope (Thermo Fisher Scientific).

Statistical Analysis: Statistical analysis of all numerical data was carried out using GraphPad Prism software (version 8). The sample size was a minimum of three replicates. Data are presented as the means  $\pm$  SEM.

**ADVANCED** SCIENCE NEWS

www.advancedsciencenews.com



www.advhealthmat.de

An unpaired two-tailed Student's t-test was used for two-group comparisons. For multiple group comparisons, ANOVA followed by Tukey's post hoc test was performed. One-way ANOVA was used for single-factor analysis and two-way ANOVA for multifactor analysis. Statistical significance is denoted as:  ${}^*p < 0.05$ ,  ${}^{**}p < 0.01$ ,  ${}^{***}p < 0.001$ , and  ${}^{****}p < 0.0001$ .

Ethics Approval Statement: All experimental procedures were conducted in accordance with the guidelines of the University of California, Los Angeles Animal Care and Use Committee and approved by the UCLA Animal Ethics Committee (Los Angeles, California, USA). The approval reference numbers were 18–043 for the tissue-sharing program and ARC-2022-106 for the biocompatibility study. No human participants were involved in this study.

#### **Supporting Information**

Supporting Information is available from the Wiley Online Library or from the author.

#### Acknowledgements

Additional members of Dr. Sturm's mentorship team included Dr. Isla Garraway, Professor of Urology at UCLA; Dr. Arun Sharma, Research Assistant Professor of Urology and Biomedical Engineering at Northwestern University Feinberg School of Medicine; and Dr. Ali Khademhosseini, Professor and CEO of the Terasaki Institute for Biomedical Innovation. Figure 1 and the table of contents were created using https://BioRender.com.

#### **Conflict of Interest**

R. Sturm is President and Co-Founder of Surgi-Zipper, Inc., a small business focused on developing LUT biodegradable adhesive tissue support devices. N. Annabi is a Co-Founder and holds equity in GelMEDIX Inc.

#### **Data Availability Statement**

The data that support the findings of this study are available from the corresponding author upon reasonable request.

#### Keywords

biocompatible materials, biomechanics, elastin-like polypeptides, tissue engineering, tissue scaffolds, urethral reconstruction, urinary bladder

Received: February 5, 2025 Revised: June 6, 2025 Published online:

a) K. Du, E. E. Mulroy, M. C. Wallis, C. Zhang, A. P. Presson, P. C. Cartwright, J Pediatr Surg 2015, 50, 1535; b) S. J. Kim, Q. G. Nang, A. RoyChoudhury, A. J. M. Kern, K. Sheth, M. Jacobs, D. P. Poppas, A. Akhavan, J Pediatr Urol 2022, 18, 314; c) I. Stanasel, H. K. Le, A. Bilgutay, D. R. Roth, E. T. Gonzales Jr., N. Janzen, C. J. Koh, P. Gargollo, A. Seth, J. Urol. 2015, 194; d) E. R. McNamara, M. P. Kurtz, A. J. Schaeffer, T. Logvinenko, C. P. Nelson, J Pediatr Urol 2015, 11, 209e1; e) C. J. Long, D. I. Chu, R. W. Tenney, A. R. Morris, D. A. Weiss, A. R. Shukla, A. K. Srinivasan, S. A. Zderic, T. F. Kolon, D. A. Canning, J. Urol. 2017, 197, 852; f) E. R. McNamara, A. J. Schaeffer, T. Logvinenko, C. Seager, I. Rosoklija, C. P. Nelson, A. B. Retik, D. A. Diamond, M. Cendron, J. Urol. 2015, 194, 1080.

- [2] a) J. J. E. Choi, J. Zwirner, R. S. Ramani, S. Ma, H. M. Hussaini, J. N. Waddell, N. Hammer, Clin Exp Dent Res 2020, 6, 602; b) S. Rahmati, A. Jalili, M. B. Dehkordi, M. Przedborski, Cell J. 2022, 24, 506; c) E. M. Cunnane, N. F. Davis, C. V. Cunnane, K. L. Lorentz, A. J. Ryan, J. Hess, J. S. Weinbaum, M. T. Walsh, F. J. O'Brien, D. A. Vorp, Biomaterials 2021, 269, 12065 1.
- [3] L. R. Versteegden, K. A. van Kampen, H. P. Janke, D. M. Tiemessen, H. R. Hoogenkamp, T. G. Hafmans, E. A. Roozen, R. M. Lomme, H. van Goor, E. Oosterwijk, W. F. Feitz, T. H. van Kuppevelt, W. F. Daamen, Acta Biomater. 2017, 52, 1.
- [4] Y. Y. Chan, M. I. Bury, E. M. Yura, M. D. Hofer, E. Y. Cheng, A. K. Sharma, Nat Rev Urol 2020, 17, 162.
- [5] L. Shi, V. Ronfard, Int J Burns Trauma 2013, 3, 173.
- [6] F. Yiu, V. Lee, A. Sahoo, J. Shiba, N. Garcia-Soto, G. E. Aninwene 2nd, V. Pandey, J. Wohlschlegel, R. M. Sturm, J Pediatr Urol 2024, 20, 843
- [7] A. J. Engler, S. Sen, H. L. Sweeney, D. E. Discher, Cell 2006, 126, 677.
- [8] J. S. Park, J. S. Chu, A. D. Tsou, R. Diop, Z. Tang, A. Wang, S. Li, Biomaterials 2011, 32, 3921.
- [9] H. M. Larsson, G. Vythilingam, K. Pinnagoda, E. Vardar, E. M. Engelhardt, S. Sothilingam, R. C. Thambidorai, T. Kamarul, J. A. Hubbell, P. Frey, Sci. Rep. 2018, 8, 10057.
- [10] K. Sadtler, S. D. Sommerfeld, M. T. Wolf, X. Wang, S. Majumdar, L. Chung, D. S. Kelkar, A. Pandey, J. H. Elisseeff, Semin. Immunol. 2017, 29 14
- [11] D. Jaskowak, R. Nunez, R. Ramachandran, E. Alhajjar, J. Yin, G. Guidoboni, Z. C. Danziger, Neurourol Urodyn 2022, 41, 1305.
- [12] a) Y. Igawa, J. J. Wyndaele, O. Nishizawa, Int J Urol 2008, 15, 481; b)
   S. B. Farnham, M. S. Cookson, World Journal of Urology 2004, 22, 157.
- [13] a) H. Samadian, H. Maleki, Z. Allahyari, M. Jaymand, Coord. Chem. Rev. 2020, 420, 213432; b) X. Guan, M. Avci-Adali, E. Alarcin, H. Cheng, S. S. Kashaf, Y. Li, A. Chawla, H. L. Jang, A. Khademhosseini, Biotechnol. J. 2017, 12, 1600394.
- [14] E. M. Carvalho, S. Kumar, Acta Biomater. 2023, 163, 146.
- [15] S. J. Buwalda, K. W. Boere, P. J. Dijkstra, J. Feijen, T. Vermonden, W. E. Hennink, J Control Release 2014, 190, 254.
- [16] L. L. Palmese, R. K. Thapa, M. O. Sullivan, K. L. Kiick, Curr. Opin. Chem. Eng. 2019, 24, 143.
- [17] E. Shirzaei Sani, R. Portillo-Lara, A. Spencer, W. Yu, B. M. Geilich, I. Noshadi, T. J. Webster, N. Annabi, ACS Biomater. Sci. Eng. 2018, 4, 2528
- [18] M. Zamani, N. Shakhssalim, S. Ramakrishna, M. Naji, Front Bioeng Biotechnol 2020, 8, 579925.
- [19] K. Zhang, Q. Fu, J. Yoo, X. Chen, P. Chandra, X. Mo, L. Song, A. Atala, W. Zhao, Acta Biomater. 2017, 50, 154.
- [20] B. J. Klotz, D. Gawlitta, A. Rosenberg, J. Malda, F. P. W. Melchels, Trends Biotechnol. 2016, 34, 394.
- [21] K. Yue, G. Trujillo-de Santiago, M. M. Alvarez, A. Tamayol, N. Annabi, A. Khademhosseini, *Biomaterials* 2015, 73, 254.
- [22] Y. N. Zhang, R. K. Avery, Q. Vallmajo-Martin, A. Assmann, A. Vegh, A. Memic, B. D. Olsen, N. Annabi, A. Khademhosseini, Adv. Funct. Mater. 2015, 25, 4814.
- [23] S. Mohanto, S. Narayana, K. P. Merai, J. A. Kumar, A. Bhunia, U. Hani, A. Al Fatease, B. H. J. Gowda, S. Nag, M. G. Ahmed, K. Paul, L. K. Vora, Int. J. Biol. Macromol. 2023, 253, 127143.
- [24] S. R. MacEwan, A. Chilkoti, Biopolymers 2010, 94, 60.
- [25] F. Ajalloueian, G. Lemon, J. Hilborn, I. S. Chronakis, M. Fossum, Nat Rev Urol 2018, 15, 155.
- [26] S. Sharma, B. Basu, Biomaterials 2022, 281, 121331.
- [27] S. Sharma, S. Rajani, J. Hui, A. Chen, T. Bivalacqua, A. Singh, ACS Appl. Mater. Interfaces 2022, 14, 37301.
- [28] M. Goedegebuure, M. I. Bury, X. Wang, P. Sanfelice, F. Cammarata, L. Wang, T. T. Sharma, N. Rajinikanth, V. Karra, V. Siddha, A. K. Sharma, G. A. Ameer, *Bioact Mater* 2024, 41, 553.

- [29] M. V. Amesty, C. I. Chamorro, P. Lopez-Pereira, M. J. Martinez-Urrutia, B. Sanz, S. Rivas, R. Lobato, M. Fossum, Front Pediatr 2021, 9, 691131.
- [30] S. S. Mahdavi, M. J. Abdekhodaie, S. Mashayekhan, A. Baradaran-Rafii, K. Kim, *Mater. Today Commun.* 2021, 27, 102459.
- [31] F. Fan, S. Saha, D. Hanjaya-Putra, Front Bioeng Biotechnol 2021, 9, 718377
- [32] J. L. Drury, D. J. Mooney, Biomaterials 2003, 24, 4337.
- [33] H. Mndlovu, P. Kumar, L. C. du Toit, Y. E. Choonara, npj Materials Degradation 2024, 8, 66.
- [34] A. Yeboah, R. I. Cohen, C. Rabolli, M. L. Yarmush, F. Berthiaume, Biotechnol. Bioeng. 2016, 113, 1617.
- [35] L. Martinez-Vidal, M. Chighizola, M. Berardi, E. Alchera, I. Locatelli, F. Pederzoli, C. Venegoni, R. Lucianò, P. Milani, K. Bielawski, A. Salonia, A. Podestà, M. Alfano, Commun. Biol. 2023, 6, 217.
- [36] H. K. Lin, S. Y. Godiwalla, B. Palmer, D. Frimberger, Q. Yang, S. V. Madihally, K. M. Fung, B. P. Kropp, Tissue Eng Part B Rev 2014, 20, 73.
- [37] A. Al Halawani, L. Abdulkhalek, S. M. Mithieux, A. S. Weiss, Biomolecules 2021, 11.
- [38] I. Noshadi, S. Hong, K. E. Sullivan, E. Shirzaei Sani, R. Portillo-Lara, A. Tamayol, S. R. Shin, A. E. Gao, W. L. Stoppel, L. D. Black III, A. Khademhosseini, N. Annabi, *Biomater. Sci.* 2017, 5, 2093.
- [39] J. W. Nichol, S. T. Koshy, H. Bae, C. M. Hwang, S. Yamanlar, A. Khademhosseini, *Biomaterials* 2010, 31, 5536.
- [40] M. Lin, S. Rose-John, J. Grötzinger, U. Conrad, J. Scheller, *Biochem. J.* 2006, 398, 577.
- [41] G. Unal, J. Jones, S. Baghdasarian, N. Kaneko, E. Shirzaei Sani, S. Lee, S. Gholizadeh, S. Tateshima, N. Annabi, *Bioeng. Transl. Med.* 2021, 6, 10240

- [42] a) A. Roy, S. Zenker, S. Jain, R. Afshari, Y. Oz, Y. Zheng, N. Annabi, Adv. Mater. 2024, 36, 2404225; b) S. Lee, E. S. Sani, A. R. Spencer, Y. Guan, A. S. Weiss, N. Annabi, Adv. Mater. 2020, 32, 2003915.
- [43] D. M. Tian, H. H. Wan, J. R. Chen, Y. B. Ye, Y. He, Y. Liu, L. Y. Tang, Z. Y. He, K. Z. Liu, C. J. Gao, S. L. Li, Q. Xu, Z. Yang, C. Lai, X. J. Xu, C. S. Ruan, Y. S. Xu, C. Zhang, L. Luo, L. P. Yan, *Mater Today Bio* 2022, 15, 100300
- [44] a) H. E. Rahardjo, V. Märker, D. Tsikas, M. A. Kuczyk, S. Ückert, A. Bannowsky, J Clin Med 2023, 12; b) I. M. Margulies, M. Höyhtyä, C. Evans, M. L. Stracke, L. A. Liotta, W. G. Stetler-Stevenson, Cancer Epidemiol Biomarkers Prev 1992, 1, 467; c) N. Gruba, L. Stachurski, A. Lesner, J. Biochem. 2021, 170, 547; d) C. B. Wilson, J. Leopard, R. M. Nakamura, D. A. Cheresh, P. C. Stein, C. L. Parsons, J. Urol. 1995, 154, 1222.
- [45] P. Sangkum, F. A. Yafi, H. Kim, M. Bouljihad, M. Ranjan, A. Datta, S. H. Mandava, S. C. Sikka, A. B. Abdel-Mageed, K. Moparty, W. J. Hellstrom, *Urology* 2015, 86, 647e1.
- [46] X. Zhao, X. Sun, L. Yildirimer, Q. Lang, Z. Y. W. Lin, R. Zheng, Y. Zhang, W. Cui, N. Annabi, A. Khademhosseini, *Acta Biomater.* 2017, 49, 66.
- [47] a) X. Song, C. Zhu, D. Fan, Y. Mi, X. Li, R. Z. Fu, Z. Duan, Y. Wang, R. R. Feng, *Polymers* 2017, 9, 638; b) M. Wang, P. Zhai, X. Chen, D. J. Schreyer, X. Sun, F. Cui, *Tissue Eng.*, *Part B* 2011, 17, 177.
- [48] I. C. Biotech, Cook Biotech, Inc., 2024.
- [49] N. F. Davis, A. Callanan, B. B. McGuire, H. D. Flood, T. M. McGloughlin, *Urology* 2011, 77, 1007e1.
- [50] A. K. Sharma, P. V. Hota, D. J. Matoka, N. J. Fuller, D. Jandali, H. Thaker, G. A. Ameer, E. Y. Cheng, *Biomaterials* 2010, 31, 6207